④

DTIC FILE COPY

Electron Spectroscopy Data for the High-Temperature
Superconductors. What can We Learn from it?

By

D. E. Ramaker

Prepared for Publication

in the

ACS Symposium Series 377

George Washington University
Department of Chemistry
Washington, D.C.   20052

December, 1988

AD-A201 985

DTIC
ELECTE
DEC 1 9 1988
H

REPORT DOCUMENTATION PAGE

1a. REPORT SECURITY CLASSIFICATION Unclassified		1b. RESTRICTIVE MARKINGS		
2a. SECURITY CLASSIFICATION AUTHORITY		3. DISTRIBUTION / AVAILABILITY OF REPORT Approved for Public Release, distribution Unlimited.		
2b. DECLASSIFICATION / DOWNGRADING SCHEDULE				
4. PERFORMING ORGANIZATION REPORT NUMBER(S) Technical Report # 46		5. MONITORING ORGANIZATION REPORT NUMBER(S)		
6a. NAME OF PERFORMING ORGANIZATION Dept. of Chemistry George Washington Univ.	6b. OFFICE SYMBOL (If applicable)	7a. NAME OF MONITORING ORGANIZATION Office of Naval Research (Code 413)		
6c. ADDRESS (City, State, and ZIP Code) Washington, D.C. 20052		7b. ADDRESS (City, State, and ZIP Code) Chemistry Program 800 N. Quincy Street Arlington, VA 22217		
8a. NAME OF FUNDING / SPONSORING ORGANIZATION Office of Naval Research	8b. OFFICE SYMBOL (If applicable)	9. PROCUREMENT INSTRUMENT IDENTIFICATION NUMBER Contract N00014-80-K-0852		
8c. ADDRESS (City, State, and ZIP Code) Chemistry Program 800 North QUINCY, Arlington, VA 22217		10. SOURCE OF FUNDING NUMBERS		

		PROGRAM ELEMENT NO.	PROJECT NO.	TASK NO. PP	WORK UNIT ACCESSION NO
		61153 N		013-08-01	NR 056-681

11. TITLE (Include Security Classification) Electron Spectroscopy Data for the High-Temperature Superconductors. What can We Learn from it?

12. PERSONAL AUTHOR(S) D. E. Ramaker

13a. TYPE OF REPORT Interim Technical	13b. TIME COVERED FROM _____ TO _____	14. DATE OF REPORT (Year, Month, Day) December 1988	15. PAGE COUNT 13

16. SUPPLEMENTARY NOTATION Prepared for publication in ACS Symposium Series 377

17. COSATI CODES			18. SUBJECT TERMS (Continue on reverse if necessary and identify by block number)
FIELD	GROUP	SUB-GROUP	Superconductivity, Photoelectron Spectroscopy, Auger Spectroscopy, Hubbard Model, Copper ox opes. (Mgnu)

19. ABSTRACT (Continue on reverse if necessary and identify by block number)

An interpretation of spectroscopic data for the high temperature superconductors utilizing a highly correlated CuO_n^n cluster model shows that a single set of Hubbard parameters predicts all of the state energies. Differences in the data from that for CuO are attributed to an increased Cu-O covalency in the superconductors. The reported temperature effects are attributed to increased metallic screening at lower temperatures.

20. DISTRIBUTION / AVAILABILITY OF ABSTRACT ☐ UNCLASSIFIED/UNLIMITED ☒ SAME AS RPT. ☐ DTIC USERS	21. ABSTRACT SECURITY CLASSIFICATION Unclassified	
22a. NAME OF RESPONSIBLE INDIVIDUAL Dr. David L. Nelson	22b. TELEPHONE (Include Area Code) (202) 696-4410	22c. OFFICE SYMBOL

DD FORM 1473, 84 MAR 83 APR edition may be used until exhausted. All other editions are obsolete.

Chapter 7

Electron Spectroscopic Data
for High-Temperature Superconductors

David E. Ramaker

Department of Chemistry, George Washington University,
Washington, DC 20052

An interpretation of spectroscopic data for the high
temperature superconductors utilizing a highly correlated
CuO_a cluster model shows that a single set of Hubbard
parameters predicts all of the state energies. Differences
in the data from that for CuO are attributed to an
increased Cu-O covalency in the superconductors. The
reported temperature effects are attributed to increased
metallic screening at lower temperatures.

An abundance of electron spectroscopic data has been reported for
the high temperature superconductors. These include the valence
band (VB), Cu 2p, and O 1s photoelectron (UPS and XPS) data, the
$L_{23}VV$ and $L_{23}M_{23}V$ Auger (AES) data, the O K and Cu L_{23} x-ray
emission (XES) data, and the O K and Cu L_{23} electron energy loss
(EELS) and x-ray absorption near edge structure (XANES) data.
These data reflect 1-, 2-, and 3-valence hole and core-hole density of
states (DOS) and therefore can provide direct measures of the
Hubbard U and transfer parameters. Unfortunately, this data has
proved to be difficult to interpret; not surprisingly since the data
for CuO is not even well understood.

Recently we consistently interpreted these data within a cluster
model assuming a highly correlated system (1,2). Here, we review the
previously reported experimental spectra for polycrystalline and
single crystal samples of $La_{2-x}Sr_xCuO_4$ or $YBa_2Cu_3O_{7-x}$ (herein
referred to as the La and 123 superconductors (HTSC's)), and
compare them with CuO. We also review our interpretation of this
data. Previously unassigned features are identified and some are
assigned differently from that given by others (3). We also obtain
the magnitudes of the U parameters. Knowledge of these magnitudes
are important for understanding the possible mechanisms involved;
for example, the resonating valence bond (4), exitonic (5), super-
exchange (6), and Coulombic (7) pairing mechanisms depend critically
on these U's.

The basic VB electronic structure of the HTSC's can be
described by a simple LCAO-MO (i.e. tight-binding) or Hubbard model,
characterized by the transfer or covalent interaction t, the Cu and O

orbital energies c_d and c_p, the intra-site Coulomb repulsion energies U_d and U_p, and the intra-site core polarization energies Q_d and Q_p. We also include the inter-site repulsion energies U_{dp} and U_{pp}° (i.e. between neighboring Cu-O and O-O atoms). An important parameter is the difference between c_d and c_p, namely $\Delta = c_p - c_d$.

All of the spectroscopic data can be understood within a $CuO_n^{(2n-2)-}$ cluster model, which is valid when the U's are large relative to the bandwidths (8,9), i.e. when correlation effects dominate covalent or hybridization effects. Both La and CuO contain CuO_6 groups (10), having 4 short and 2 long Cu-O bonds. The 123 HTSC contains CuO_5 and planar CuO_4 groups (10). The different n may alter the relative intensities of various features as pointed out below, but similar features are present in each case. The different bond lengths may increase the widths of the spectral features, but little else since correlation dominates.

Although relatively isolated CuO_2 planes exists in the HTSC's, the CuO_n clusters are not isolated, for most of the O atoms actually are part of two CuO_n clusters. Consistent with previous work (7), we account for this by defining the effective parameter, $c_p = c_p' + U_{pe}$, where U_{pe} includes the interaction of a hole in an O p orbital with its environment, i.e. with the neighboring Cu atom or cluster. If for example each of the neighboring Cu atoms contains a hole (we shall see below that this is essentially the ground state), U_{pe} will equal U_{dp}. But in general, U_{pe} will be smaller than U_{dp} due to polarization of the lattice. Throughout the remainder of this work, c_p is assumed to include this effect.

Since Cu atoms have the electronic configuration $3d^{10}4s^1$ and O the configuration $2s^2 2p^4$, the $CuO_n^{(2n-2)-}$ cluster has one hole shared between the Cu 3d and O 2p shells in the ground state. The various spectroscopies then reflect either v^2-, v^2-, c-, or cv- hole (c = core hole, v= valence hole) states as indicated in Table 1. We indicate the location of the holes by d (Cu 3d) or p (O 2p). In the case of two holes on the oxygens, we distinguish two holes on the same O (p^2), on ortho neighboring O atoms (pp°), or on para O atoms (pp') of the cluster. Furthermore, neighboring pp° holes can dimerize (11-13), so we distinguish between two holes in bonded (pp°$_b$) and antibonded (pp°$_a$) O pairs, i.e. the same or different O_2 dimers. Both the doped La and 123 materials contain additional holes which serve as the charge carriers, and some spectroscopies reflect these directly.

Table 1 contains the estimates of the Hubbard parameters which together provide the best agreement with the state energies as reflected in the spectra and the theoretical DOS. The energies relative to the ground state are given in terms of the Hubbard c and U parameters defined above. The agreement of the estimated energies with the spectral features is also shown in Table 1. We discuss the assignment of the spectral features below.

The Theoretical DOS

The v states are best reflected by the highly accurate theoretical DOS (14), which for the HTSC's can qualitatively be described as des having the Cu-O bonding ($\downarrow_b$) and antibonding ($\downarrow_a$) orbitals centered at 4 and 0 eV and the nonbonding Cu and O orbitals at 2 eV. The O features each have a width $2\Gamma = 4$ eV due to the O-O bonding and

TABLE 1 Summary of hole states revealed in the spectroscopic data, and estimated energies using the following optimal values for the Hubbard parameters in eV[a]:

$\delta_1 = 2$ $\epsilon_d = 2$ $U_p = 12, 13$ $U_d = 9.5, 10.2$

$\delta_2 = 0.5, 0.8$ $\epsilon_p = 2, 3$ $U_{pp}{}^\bullet = 4.5, 4$ $U_{dp} = 1$

$\Gamma = 2$ $U_{pp}{}^{\bullet\bullet} = 0.$ $U_{cp}{}^\bullet = 2$ $Q_d = 9$

$\alpha = 1, 0.5$ $\beta = 2$ $\Delta = 0, 1.$ $K = 4$

State[b]	Energy expression	Calc. E. eV[c,d]	Exp. E. eV[c]	Remark
	G.S. and IPES, v			
$\dagger_a$) d	$\epsilon_d - \delta_1 \mp \Gamma$	0 ∓ 2	–	⎤ heavily
$\dagger_b$) p	$\epsilon_p + \delta_1 \mp \Gamma$	4 ∓ 2	–	⎦ mixed
	UPS and XES, v[2]			
1)[•] pp[•]	$\epsilon_p + \Delta - \delta_2 + \alpha$	2.5	2.5	⎤ heavily
2)[•] dp	$\epsilon_p + U_{dp} + \delta_2 + \alpha$	4.5	4.2	⎦ mixed
3) pp[•]$_a$	$\epsilon_p + \Delta + U_{pp}{}^\bullet - \Gamma + \alpha$	5.5	5.	
4) pp[•]$_b$	$\epsilon_p + \Delta + U_{pp}{}^\bullet + \Gamma + \alpha$	9.5	9.5	mystery peak
5) d[2]	$\epsilon_d + U_d + \alpha$	12.5	12.5	Cu sat.
6) p[2]	$\epsilon_p + \Delta + U_p + \alpha$	15	16	
	Cu 2p XPS, cv			
d → cp	$\epsilon_c + \Delta + \alpha$	$\epsilon_c + 1$	E_{2p}	main
cd	$\epsilon_c + Q_d + \alpha$	$\epsilon_c + 10$	$E_{2p} + 9.2$	sat.
	Cu 2p XPS for NaCuO$_2$, pp[•] → cv[2]			
pp[•]→cpp[•]	$\epsilon_c + \delta_2 + \beta$	$\epsilon_c + 2.5$	$\epsilon_c + 2.2$	main
cpp[•]$_a$	$\epsilon_c + U_{pp}{}^\bullet - \Gamma + \delta_2 + \beta$	$\epsilon_c + 4.5$	$\epsilon_c + 5$	?
cpp[•]$_b$	$\epsilon_c + U_{pp}{}^\bullet + \Gamma + \delta_2 + \beta$	$\epsilon_c + 8.5$	$\epsilon_c + 9$	?
cdp	$\epsilon_c - \Delta + Q_d + U_{dp} + \delta_2 + \beta$	$\epsilon_c + 11.5$	$\epsilon_c + 11$	sat.
cp[2]	$\epsilon_c + U_p + \delta_2 + \beta$	$\epsilon_c + 15.5$	$\epsilon_c + 14$	sat.?
	O 1s XPS, cv			
d → cd	$\epsilon_c + \alpha$	$\epsilon_c + 1$	E_{1s}	main
cp[•]	$\epsilon_c + \Delta + \alpha$	$\epsilon_c + 1$	E_{1s}	main
cp[•]	$\epsilon_c + \Delta + U_{cp}{}^\bullet + \alpha$	$\epsilon_c + 3$	$E_{1s} + 2$?	tail
cp	$\epsilon_c + \Delta + Q_p + \alpha$	?	?	not obs.
pp[•]→cdp[•]	$\epsilon_c - \Delta + U_{dp} + \delta_2 + \beta$	$\epsilon_c + 3.5$	$E_{1s} + 2$?	tail
	Cu L$_3$VV AES, v[2]			
dpp[•]	$2\epsilon_p + 2U_{dp} + \alpha$	7	7	2 cent.
dpp[•]	$2\epsilon_p + U_{pp}{}^\bullet + 2U_{dp} + \alpha$	11.5	–	no mix
d[2]p	$\epsilon_d + \epsilon_p + U_d + 2U_{dp} - \delta_2 + \alpha$	16	15.5	main
dp[2]	$2\epsilon_p + U_p + 2U_{dp} + \delta_2 + \alpha$	19.5	18-25	sat.

TABLE 1 (cont.)

State[b]	Energy expression	Calc. E. eV[c,d]	Exp. E. eV[c]	Remark
Cu L₂M₂₃V AES, cv²				
cdp	$c_c+c_p+Q_d+U_{dp}\mp K+\alpha$	c_c+9	$E_{3p}+10$	main, ¹L
		c_c+17	$E_{3p}+18$	main, ³L
cp²	$c_c+c_p+\Delta+U_p+\alpha$	c_c+15	–	]not
cd²	$c_c-c_d+U_d+2Q_d+\alpha$	$c_c+30.5$	–	]obs.
Cu L₂₃ EELS, c				
d → c	$c_c-c_d+\delta_1$	$E_{2p}-1$	$E_{2p}-1.4$	edge
cpCB	$c_c+\Delta-CB+\alpha$	$E_{2p}-CB$	$E_{2p}+1.2$	upper
pp* → cp	$c_c-c_p+\delta_2+\beta$	$E_{2p}-0.5$	E_{2p}	middle
O K EELS, c				
d → c	$c_c-c_d+\delta_1$	$E_{1s}-1$	E_{1s}	edge
cdCB	$c_c-CB+\alpha$	$E_{1s}-CB$	$E_{1s}+1.7$	upper
pp* → cd	$c_c-\Delta-c_p+\delta_2+\beta$	$E_{1s}-0.5$	–	not obs.

[a]Parameters for 123 indicated first, those for CuO second.
[b]The dominant character in the hybridized states is given.
[c]The Calc. E and Exp. E columns indicate the results for 123, except for the "Cu 2p XPS, pp* → cv²" section, which is for NaCuO₂.
[d]The calculated E is defined relative to the ground v^1 (d) state energy $= c_d - \alpha$, or to the v^2 (pp*) ground state energy $= 2c_p-\delta_2-\beta$. The v^1(d) energy defines the Fermi level relative to the vacuum level at zero.
[e]The dominant character switches as described in the text, and thus the sign in front of δ_2 is the opposite for CuO.

antibonding character and the Cu–O dispersion. The $\dagger_b$ and $\dagger_a$ wavefunctions can be expressed as (8,9),

$$\dagger_a = d \cos\vartheta_1 - p \sin\vartheta_1 \qquad (1a)$$
$$\dagger_b = d \sin\vartheta_1 + p \cos\vartheta_1 \qquad (1b)$$

where $\vartheta_1 = 0.5 \tan^{-1}(2t/\Delta)$. We also define the Cu–O hybridization shift $\delta_1 = 0.5 \sqrt{\Delta^2+4t^2} - \Delta/2$, which is utilized in Table 1 to give the energies. In this picture, the ground state of an average CuO$_6$ cluster is located at 1 eV having the energy $\epsilon_d-\delta_1+\Gamma/2 = \epsilon_d-\alpha$, which we use as a reference energy for all of the higher v^a states. Similarly, the inverse photoemission data (e.g. see Fig. 4c), which reflects the unoccupied v DOS, gives a feature at $\epsilon_d-\delta_1-\Gamma/2 = -1$ eV, due to the simultaneous Cu–O and O–O antibonding orbitals. Above, α is the average hybridization energy shift in the ground state of a CuO$_6$ cluster. We ignore the O–O hybridization shift for all of the excited states, except for the pp^o states, where it is large.

The DOS for CuO is in fact less well characterized than for the HTSC's theoretically, but generally the hybridization shift Γ is smaller because of the larger O–O distances, and we shall see below that $\Delta=\epsilon_p-\epsilon_d$ has increased to 1 eV. This increase can be attributed to an increase in ϵ_p, or U_{pd}, and reflects a smaller lattice polarization response due to the more ionic character in CuO.

The VB UPS and XPS Data

The photoemission process involves excitation from the v to the v^a states. The six different v^a states in Table 1 have a large energy spread. States 1,2,5 & 6 have the same symmetry and mix together; unfortunately, the result cannot be given simply in analytical form as above. The two pp^o states (3 & 4) have different symmetry and mix separately. Only states 1 & 2 and 3 & 4 are heavily mixed so that they are the only ones to experience a significant hybridization shift, δ_2 and Γ, as shown in Table 1. The sudden approximation and the cross-sections for ionization from the O 2p and Cu 3d shells, σ_p and σ_d, can be utilized to give the expected relative photoemission intensities for the six v^a states. σ_p and σ_d are known to be approximately equal around 40 eV, with σ_d larger above this, and σ_p larger below this energy (i.e. σ_p/σ_d is roughly 2. for 21 eV, 1. for 45, and 0.3 for 100 eV photons (14)). The photon dependence of the UPS data can be understood from the variation in the cross-sections, and from the realization that at low photon energies, the sudden approximation breaks down. The opposite extreme, the adiabatic limit, gives intensity only in the lowest state of each symmetry, 1 and 3, since the system is able to relax before escape of the photoelectron. UPS spectra reflect the case somewhere between these limits.

The valence band features. Examination of the UPS data in Figure 1b shows two features at 3 and 5.5 eV for CuO (15,16) and three for the superconductors (17) at 2.5, 4.2, and 5 eV, which obviously result from the hybridized states 1-3. Photon energy dependent data in Figure 1 shows that the features around 5.5 eV in CuO and 2.5 and 5 eV in 123 arise more from σ_p, and the feature at 3 in CuO and 4.2 eV in 123 from σ_d (17-22). In CuO, we assign the 5.5-eV feature to pp^o_a and pp^p and the 3-eV to dp. In 123, we assign the 5-eV to pp^o_a,
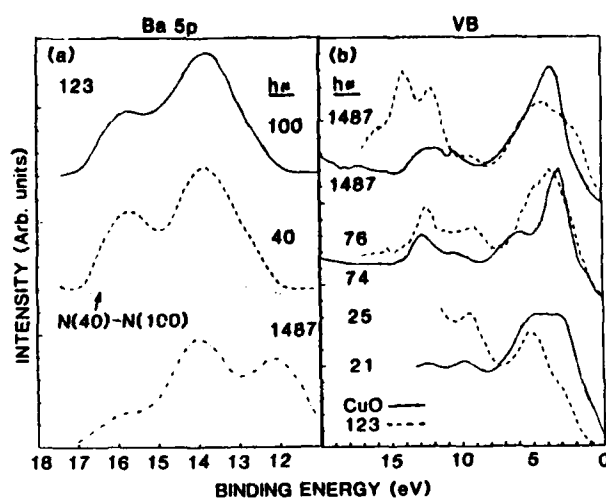
Figure 1a. Comparison of photoelectron spectra in the range 11-18 eV for 123 . Data from refs. 17 (hv = 100 and 40) and 24 (hv = 1487).

1b. Comparison of UPS spectra for CuO and 123 taken with the indicated photon energies in eV. Data for CuO from refs. 23 (hv = 1487), 15 (hv = 74) and 16 (hv = 21). Data for 123 from ref. 17 (hv = 25 and 74) and 24 (hv = 1487).

(Reproduced from Ref. 1, Not subject to copyright.)

the 4.2 to dp and the 2.5 to pp*, where we indicate the dominant character of each hybridized state. Calculated photoemission intensities and their variation with Δ further confirm these assignments (1).

The character switch of state 1 from mostly dp to pp* and vice versa for state 2 between CuO and 123 arises because Δ decreases from 1 eV in CuO to 0 eV in 123. The reduction in Δ, due to reduction in ϵ_p or U_{pp}, is consistent with the Cu 2p XPS data and with the XES data to be discussed below; the latter very dramatically reveals this character switch. States 1 and 2 remain a few eV apart in spite of this switch because of the heavy CI mixing. Since state 1 is primarily of pp* character in the HTSC's, the additional "charge carrier holes" (present in the La after Sr doping and in the 123 when 7-x is greater than 6.5) are primarily on the oxygens. We use this "pp*" state as the ground state for those CuO_a clusters containing two holes.

Angle resolved PES data on single crystals of 123 show that the 2.5 eV feature is the only one which shows significant angular dispersion and a photon energy dependence (17). Its angular dispersion of 0.25–0.3 eV is much smaller than the 2 eV expected from band calculations (14). The near lack of dispersion is consistent with our highly correlated cluster model. The small dispersion of the 2.5 eV feature probably comes from inter-CuO_4 cluster interaction, which is expected to be the largest when both holes are on the bordering O atoms. The region within 1 eV of E_f is free of photoyield for $h\nu = 30$ eV, but has a substantial yield for $h\nu = 18$ eV; indeed it stretches up to E_f for off normal emission (17). These lower energy states reflect the average v^2 ground state, since only a small fraction of the CuO_a clusters have two holes in the ground state. Thus we use $2\epsilon_p-\delta_2-\beta$ as the energy of the pp* ground state relative to E_v, where β represents the 2 eV energy shift between the principal pp* UPS final state at 2.5 eV and the lowest pp* states around 0.5 eV from the Fermi level.

The d^2 satellite. The principal multiplet of the d^2 final state for CuO is known to fall at 12.5 with a smaller one around 10 eV (15). The intensity of the d^2 final state can be enhanced by the Cu 2p → 3d resonant excitation process followed by an Auger decay (15). This process is resonant between 72–80 eV. The HTSC's exhibit a similar behavior (18). The satellites in Cu_2O and Cu do not have non-resonant components (15) because the UPS for Cu_2O and Cu reflect the one-hole DOS. However, the VB XPS of CuO and the HTSC's can and do show a significant nonresonant d^2 satellite (see Figure 1) (23); indeed, it should grow as one approaches the sudden limit. This possibility makes it even more difficult to interpret the XPS data for the HTSC's, since the d^2 satellite at 12.5 in the VB XPS falls at or near the same energy as the Ba spin-orbit split 5p features, which have been very controversial.

For the XPS (Figure 1a), Miller et al (24) have indicated that the 12.5 eV feature results from the Ba representative of the bulk, and the 14 and 16 eV features result from Ba bonded to OH⁻ and CO_3^- on the surface. Steiner et al (25) indicate that the 12.5 eV feature is representative of those Ba atoms surrounded by O atoms, but that the 14 and 16 eV features arise from those Ba atoms with either neighboring O defects or O atoms with holes (i.e. O⁻ instead of

O^{2-}). Recent data (17) on single crystals cleaved in-situ, when impurities are not expected, reveal the 14 and 16 eV features at glancing emission (i.e. representative of the surface), and two additional features shifted up by about 1 eV at normal emission (i.e. more representative of the bulk). This shift has been interpreted as a surface chemical shift, but it is actually consistent with the Steiner data and interpretation, if one assumes more O defects exist at the surface. Recently Weaver et al (26) reported XPS data for sintered 123, which actually reveal only the features at 12.5 and 14 eV. This indicates either that their surface is free of impurities or that the bulk and surface is totally oxidized (i.e. within the Miller or Steiner interpretations). More experimental data is required here to conclusively decide on these two alternatives and to determine what part if any of the 12.5 eV feature results from the d^2 satellite. In our opinion, the Steiner interpretation appears the more plausible at this time.

The pp^*_b feature. The pp^*_b state is believed to be responsible for the "mystery" peak found at 9.5 eV in the UPS. Although some earlier reports suggested that this feature might result from impurities such as carbon on the surface (27), more recent single crystal data (17) as well as sintered powder data (22) (Figure 1b) indicate that it is intrinsic to the material . Comparison of the UPS (15,16) in Figure 1 for photon energies of 74 and 21 eV indicates that such a feature also appears for CuO. Thus this feature is not unique to the HTSC's. It does not appear for Cu_2O, as expected since UPS reflects the one-hole DOS in Cu_2O.

UPS data indicate that the 9.5 eV feature has a cross-sectional dependence similar to σ_p (19-22), consistent with the pp^* identification. This feature cannot arise from the p^2 final state because U_p is around 12-13 eV, much too large to cause a feature at 9.5 eV. An upper estimate of the two-center pp^* hole-hole repulsion, U_{pp}^*, can be obtained from the Klopman approximation (28),

$$U_{ij} = e^2/(r_{ij}^2 + (2e^2/(U_i + U_j))^2)^{1/2} \tag{2}$$

where r_{ij} is the interatomic distance and U_i and U_j are the corresponding intra-atomic repulsion energies. Equation 2 gives a value for U_{pp}^* around 4.8 eV, assuming the O-O distance is 2.7 A$^\circ$. The experimental energies of 9.5 and 5.0 eV for pp^*_b and pp^*_a in 123 suggests that the average pp^* final state energy is 7.2 eV. This gives an empirical estimate for U_{pp}^* of 4.2 eV, close to the Klopman theoretical result, which does not include the effects of interatomic screening.

The above result shows that metallic screening of two holes, which are spatially separated on neighboring O atoms, is not very significant. This is in contrast to two Cu-O holes, where Table 1 indicates the optimal $U_{dp} = 1$ eV, while eq. 2 estimates U_{dp} at 6.1 eV, assuming an average Cu-O distance of 1.9 A$^\circ$. This large reduction in U_{dp} probably results from charge transfer into the Cu 4sp levels to screen the Cu-O holes. Although metallic screening, which results from virtual electron-hole (e-p) pair excitations at the Fermi level, is not expected to be large in an insulator such as CuO, screening effects are expected to be much larger in metals, such as the HTSC's. The above results show that U_{dp} is significantly reduced in both,

and $U_{pp}°$ remains large in both. The lack of a significant change in the U's between CuO and the HTSC's indicates that the DOS at the Fermi level in the HTSC's must be very small.

The assignment of the 9.5 eV feature explains some of its interesting characteristics. Comparison of data (19) for $YBa_2Cu_3O_x$ (123$_x$) ·with O levels at x = 6.95, 6.5, and 6.05 reveal that the reduced O materials, 123$_{6.5}$ and 123$_{6.05}$, have two peaks around 9.4 and 11.5 eV. It is known that the oxygen decrease resulting from quenching or heating in vacuum occurs primarily from the CuO_4 chains (29). This may leave distorted CuO_x or even peroxide O_2^- clusters (11-13) which have an O–O distance less than that in the ordered CuO_4 groups, and hence a larger $U_{pp}°$. A $U_{pp}°$ of 6.5 eV requires an O–O distance of less than 2 A°. Very recent data (30) on the new Bi and Th type HTSC's indicate a single feature at around 10 eV, consistent with the 123 material.

The p^2 feature. Evidence for the existence of the p^2 feature, estimated to appear at 17.5 eV can indeed be found around 17 eV in the XPS for CuO in Figure 1. In the HTSC's, the Ba 5d peaks fall in this region, making it more difficult to identify the d^2 feature. Nevertheless, recent UPS data on single crystal 123 materials may reveal the p^2 feature (17). Figure 1 shows UPS at hν = 100 and 40 eV. An interesting change in the relative intensity of these two peaks is found, when normally one would expect the relative intensity of the $5p_{1/2}$ and $5p_{3/2}$ peaks to remain constant with photon energy. But, the 40 eV spectrum should have a larger σ_p contribution. This suggests that the hν = 40 eV spectrum may have a contribution from the p^2 state, such as that indicated in Figure 1.

The Cu 2p and O 1s XPS Data.

The Cu 2p XPS. The Cu 2p and O 1s XPS data for CuO and the 123 or La materials are shown in Figure 2 (31,32). The primary and satellite features in the Cu spectrum are known to arise from the cp and cd states, respectively (8), having the energies given in Table 1. The relative satellite intensity, I_s/I_m decreases from 0.55 in CuO to 0.37 in 123 as determined from the experimental data (33). The energy separation, $E_{sat} - E_m$ increases from 8.7 eV in CuO to 9.2 in 123 (33). These changes are just that expected for a decrease in c_p and a possible increase in t_1. These changes reflect an increased covalency in 123.

In the sudden approximation, the satellite intensity increases with change in the hybridization between the v and cv states. In the ground v state, the hole is primarily in the d orbital, in the primary cv state it is mostly in the p orbital. However, some hybridization still occurs among the cv states, since the large width of the primary cp peak is believed to arise from the mixing with the cd state. The cd state has a large width due to the large core-hole, valence-hole interaction, indeed, the satellite actually reveals the cd multiplet structure. Evidence that the primary cp peak width arises from the cd interaction comes from the Cu halide data (8), as well as the different Cu oxide data in Fig. 2a, which show a direct correlation of the primary cp peak width with the satellite cd peak intensity. We do not believe that the primary peak width arises from the O p band width as proposed by others (34).
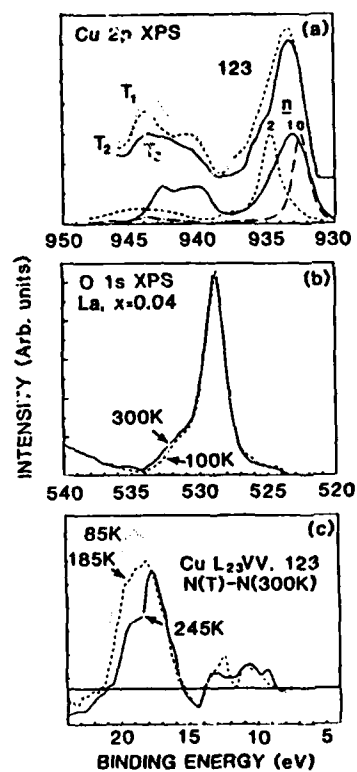
Figure 2a. Cu 2p XPS data for 123 at the temperatures 350, 230K, and 180K and denoted by T_1, T_2, and T_3 in the Figure (from Ref. 32) and for $NaCuO_2$, CuO, and Cu_2O, which reflect the cv^n (n = 2,1, and 0) DOS (from Ref.35). The energy shift seen between 123 and CuO is not real, since data taken by the same authors indicate that they agree to within 0.5 eV (35).

2b. O 1s XPS data from a single crystal La sample at the indicated temperatures (from Ref. 31).

2c. Cu $L_{23}VV$ AES difference spectra (N(T)-N(300K)) for 123 at the indicated temperatures (from Ref. 52).

(Reproduced from Ref. 1, Not subject to copyright.)

Figure 2a also contains the Cu 2p XPS spectra for Cu_2O, CuO, $NaCuO_2$ (35). These materials have the formal Cu valence of +1, +2, and +3, but in the current picture they reflect the cv^n DOS, with $n=0$, 1, and 2. Cu_2O has just a core hole c, with an energy of ϵ_c, and a negligible satellite. The primary cp feature for CuO has its energy shifted by $\Delta+\alpha$ relative to ϵ_c, and the cpp^* feature for $NaCuO_2$ by $\delta_2+\beta$ (Table 1), which is consistent with Fig. 2a. The spectrum in Fig. 2a for $NaCuO_2$ also reveals several other cv^2 features at energies consistent with Table 1. Identification of the cpp^*_a and cpp^*_b states as contributing to the features around 5 and 9 eV relative to ϵ_c is tentative. This is because the pp^* configurations do not mix significantly with the pp^* configuration in the v^2 ground state (they have different symmetry), and hence they should contribute very little intensity. The cdp satellite feature has a lower intensity in $NaCuO_2$, because the change in hybridization between the initial v^2 and final cv^2 states is not as large as for the v and cv states in CuO and the HTSC's as described above. The change in hybridization is small in $NaCuO_2$ because the pp^* and cpp^* configurations have the lowest energy in both cases.

Finally, we note that no evidence exist for the cd^2 feature, even in $NaCuO_2$, so that Cu^{3+} does not exist in either $NaCuO_2$ or in the HTSC's. Nevertheless, evidence for the presence of the cpp^* feature does appear in the spectra for 123, as shown in Fig. 2a. The magnitude of the cpp^* feature varies with the quenching temperature utilized during the processing of the samples (36,37). It has also been shown that the intensity of this feature correlates with T_c; but, the samples are still superconducting at lower T_c, even though this feature appears to be absent (36,37). At still higher quenching temperatures the material becomes a semiconductor, and the c feature appears, indicating the presence of Cu^{+1} (36).

The O 1s XPS. The O 1s spectra have been reported by many authors; however, it is seriously altered by impurities such as OH^- and CO_3^- on the surface (38–40). Recent data (31) from single crystal samples of the La material cleaved in-situ are expected to be reasonably free of impurity effects. The cp^* and cp^* states listed in Table 1 are believed to account for the tailing off of the spectra for the O 1s XPS as seen in Figure 2 (this will be positively identified upon examination of the XES data). This tailing off is much smaller in undoped La samples indicating that the $v^2 \rightarrow cv^2$ transitions also contribute in this region similar to that found in the Cu 2p XPS. Consistent with the sudden approximation, the cp state is not seen in the O 1s XPS because now both the ground v and core hole cv states have similar hybridization, i.e. the valence hole is mostly in the d orbital in both cases.

The Cu $L_{23}VV$, $L_{23}M_{23}V$, and O KVV Auger data.

The Cu $L_{23}VV$ and $L_{23}M_{23}V$ Auger data (9,33,41–43) reflect the v^3 and cv^2 DOS, respectively, and therefore provide further information on the Hubbard parameters. The L_2 and L_3 features and associated satellites are identified in Fig. 3. Table 1 indicates that the energies of these features are predicted accurately by the U and c parameters established above. We need only discuss the relative intensities.
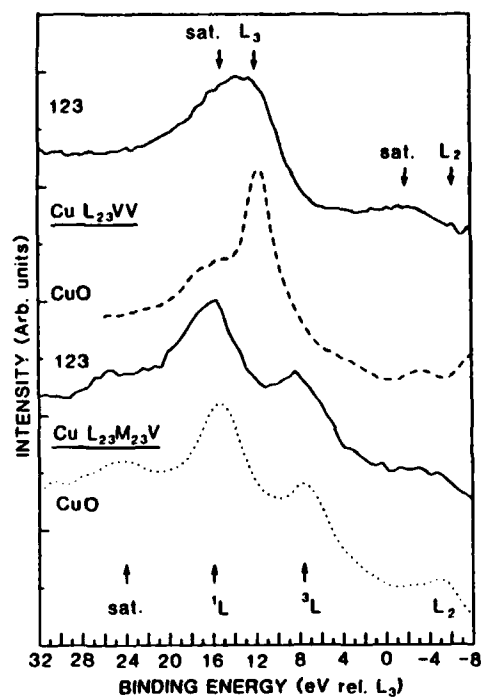
Figure 3. Comparison of Auger data for the materials indicated. $L_{23}VV$ data for CuO and 123 from ref. 49. $L_{23}M_{23}V$ data for CuO from ref. 42 and for 123 from Ref. 2. The $L_{23}VV$ data is on a 2-hole binding energy scale $= E_{L_3}-E_{k}$, and the $L_{23}M_{23}V$ on a 1-hole scale $= E_{L_3}-E_{k}-E_{M_3}$, where $E_{L_3} = 933.4$ and $E_{M_3} = 77.3$ eV (15,16). (Reproduced from Ref. 2, Not subject to copyright.)

We point out at the outset that the initial state shake-up (SU) process, which is responsible for the Cu 2p XPS satellite discussed above, does not produce a satellite in the Auger lineshape, because the cd final states resulting from this SU process "relax" to cp states before the Auger decay. This is expected because the SU excitation energy is much larger than the core level width. In contrast, the cdp states resulting from the shakeoff (SO) (g.s. + $h\nu \rightarrow$ L_3dp) and the Coster-Kronig (CK) decay (g.s. + $h\nu \rightarrow L_{11}p \rightarrow L_3$dp) processes cannot dissipate before the Auger decay, because an extra hole is present, and it is bound on the CuO_6 cluster. Thus the satellites identified in both the $L_{23}VV$ and $L_{23}M_{23}V$ lineshapes arise primarily from the initial state SO and CK processes.

Comparison of the intensities of these satellites reveals a most interesting point however. Although 123 shows an increased satellite in the $L_{23}VV$ relative to CuO, it is not increased in the $L_{23}M_{23}V$. This different behavior between the two satellites suggests strongly that the increased satellite in the L_3VV does not result from the initial state SO and CK processes, since the initial state is the same in both. Thus it must arise from a final state effect. Within our cluster model, a final state effect arises naturally from configuration mixing between the v^3 states listed in Table 1.

Since only the primary cp core-hole state Auger decays, and this process is known to be strictly intra-atomic, the $L_{23}VV$ lineshape reflects the d^2p DOS, as it is distributed among the v^3 final states. The dpp* state does not mix with d^2p since it does not have the same point group symmetry possessed by all the other v^3 final states and the cv initial state. The d^2p state at 15.5 eV is the main feature, and the dpp* state at 7 eV is what we have previously referred to as the "two center" feature (33). The dp^2 state falls on top of the satellite feature and obviously accounts for its increased intensity in 123. Its intensity is increased in 123 relative to CuO because the energy separation (before hybridization) between d^2p and dp^2 has decreased from 3.8 eV in CuO to 2.5 eV in 123. The hopping parameter t may also be increased in 123, further increasing the mixing between these two states. We have indicated this mixing in Table 1 by adding the hybridization shifts δ_2 to the energy expressions for these two states.

The $L_{23}M_{23}V$ lineshape reflects the cdp DOS. The mixing of the other states (cd^2, cpp*, cpp*$_a$, and cpp*$_b$; the latter three are not listed in Table 1) with the cdp state is small because of the large energy separations involved. The cp^2 state is close to cdp; however, it falls in between the ^3L and ^1L multiplets of the cdp state. Although it may have some intensity, it surely does not contribute to the CK + SU satellite around 25 eV in either CuO or 123. The exchange splitting (2K) between the 3p and d holes is known to be very large (8), so we include it explicitly in Table 1 to account for the $^{1,3}L$ multiplets.

The O KVV lineshape is severely altered by impurities in the sintered HTSC's, and no single crystal lineshape data have been reported. The O XVV lineshapes for CuO and Cu_2O have been reported (16), and they have the primary dp^2 or p^2 features, respectively, around 19 eV. A very small satellite appears around 7 eV in Cu_2O which we attribute to the pp* state. A much larger and broader satellite around 7 to 14 eV in CuO appears, which we attribute to the d^2p state around 14 eV as well as a smaller amount

to the dpp^p state around 7 eV. Thus the d^{2}p and dp^2 states appear in both the Cu L$_{23}$VV and O Auger lineshapes for Cu^{+2} oxides, except their primary and satellite roles are reversed.

The Cu L$_{23}$ and O K XES data

The Cu L$_{23}$ XES data (44,45) shown in Figure 4 dramatically reveals the switch in character of the 1 and 2 v^2 states between CuO and 123. As in the Auger process, the satellite cd initial state relaxes to the cp state before the decay, and the x-ray emission process is intra-atomic in nature. Therefore, the XES reflects primarily the dp DOS. In CuO the XES spectrum peaks at 3 eV, in the 123 it falls around 4.2 eV, very near where we indicated the dp states fall in the UPS data. The large intensity in the CuO XES extending above the Fermi level is believed to be an experimental artifact (45).

The O K XES data (44) confirms our assignment of the O XPS. The principal XPS peak arises from the cd state, and it decays to the dp state. Therefore the principal O XES peak aligns with the Cu XES and the dp feature in the UPS. The cp^e state does not mix with the primary cd state; therefore, it does not relax before the decay, but decays directly to the pp^e_b (and perhaps a little also to the pp^e_a) state. This accounts for the feature around 6.5 eV in the XES, just 3 eV above the pp^e_b feature in the UPS. The shift of 3 eV matches the energy difference between the cp^e and cd core hole states. The cp^p state does mix with the cd state, therefore it can relax to the cd state, but it does this slowly because of the small excitation energy of 0.5 eV. Therefore, the cp^p state decays either directly to the pp^p state, or relaxes to the cd state, which then decays to the dp state. This explains the photon energy dependence seen in the data. At high photon energy, the sudden approximation is more valid, creating a larger intensity for the cp^p state, and consequently a larger pp^p contribution around 2.5 eV in the XES.

The Cu L$_{23}$ and O K EELS and XANES Data

The EELS and XANES data in Figure 4 (46-48) reflect the contributions from three possible transitions; the dominant d $\rightarrow$ c contribution nearest the Fermi level, the pp^p $\rightarrow$ cv (v = d or p) contribution resulting from the carrier hole states, as well as the cvCB contribution well above the Fermi level (47). Here CB represents an electron present in the higher Cu 4sp or O 3p "conduction band". The latter two contributions are not always resolved, and sometimes have been confused in the literature (46-48). Although very similar, the EELS data appear to have lower resolution than the recent XANES data (48), and the EELS data may emphasize the cvCB contributions, perhaps because of a slight breakdown in the dipole approximation.

The CB DOS must reflect the presence of a core hole as dictated by the final state rule (49). The large peak at -1.7 eV in the O K for CuO and around -1.2 eV in the Cu L$_{23}$ in Figure 4 is believed to arise from these cdCB and cpCB states, respectively (47). Note that an E$_{2p}$-E$_s$ excitation energy in Table 1 corresponds to a feature at E$_s$ (binding energy) in Fig. 4. The cdCB state in CuO is excitonic-like as the O 3p DOS drops into the 2 eV gap because of the core hole. Cu$_2$O is a filled band in the ground state, so only a cCB feature appears around -1. eV. This feature in Cu$_2$O has helped
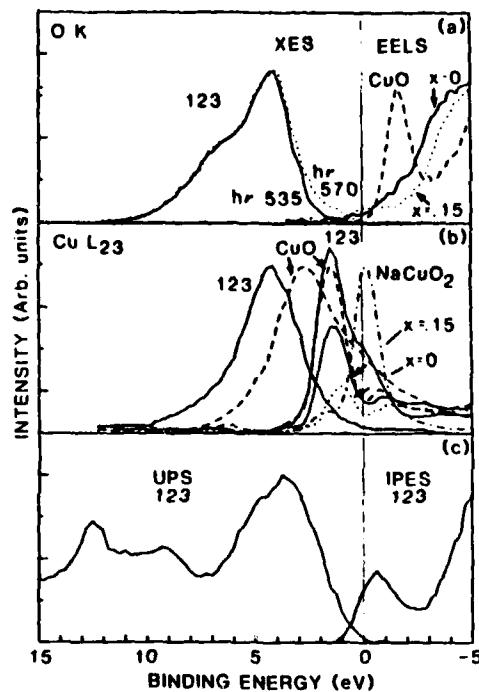
Figure 4a. Comparison of O K XES data for 123 taken at the indicated photon excitation energies (from Ref.44). Also, comparison of O K EELS data for CuO and La at the indicated Sr dopant levels (from Ref. 46)

4b. Comparison of Cu L$_{23}$ XES data for 123 (Ref. 44) and CuO (Ref. 45), of EELS data for CuO and La at the indicated Sr dopant levels (Ref. 46), and of XANES data for 123 and NaCuO$_2$ (Ref. 48).

4c. UPS (hν = 74 eV from Ref. 17) and IPES data (hν = 18 eV from Ref. 14) for 123.

(Reproduced from Ref. 2, Not subject to copyright.)

to identify the similar features in CuO and the HTSC's. The doped La material, which is metallic, does not exhibit the excitonic feature, but a cdCB contribution is still believed to be present around the same energy in the O K EELS (2).

The dominant d → c features are predicted by our model to be excitonic-like, i.e. bound by $\Delta + \alpha$ at the Cu L_{23} and by α at the O K levels. For La this is predicted to be 1 eV in both cases, however the data in Fig. 4 indicates that this is near zero at the O K. Nevertheless, our model predicts that the c states at the Cu L_{23} level should have a larger binding energy for CuO than for La (1.5 vs. 1 eV), and should be larger at the Cu L_{23} level than at the O K level for CuO (1.5 vs. 0.5 eV). Both of these trends are consistent with experiment.

The difference in the intensities of the d → c features for CuO and La can be understood by invoking the initial state rule (50). Since the c state has no valence holes, the edge features in the EELS data reflect the initial DOS as dictated by the initial state rule. We have previously proposed initial and final state rules which are appropriate for the nearly filled and empty band cases respectively (50). Here, the valence band is nearly filled while the conduction band is nearly empty; hence the c states reflect the initial v DOS, the cvCB reflect the final CB DOS. Thus the edge features in the EELS or XANES reflect directly the unfilled ground DOS, just as the inverse PES (IPES) data does in Figure 4c.

The change in intensities of the edge features between CuO and the undoped La material arises because of the smaller Δ in La. A decrease in Δ from 1 eV for CuO to significantly less than one for La means a larger probability for holes on the oxygens in the ground state of La (see eq. 1). This dictates an increase in the O K, and decrease in the Cu L_{23} d → c features compared with CuO, in agreement with experiment.

The pp* → cp contribution has been resolved as a separate feature in the recent high resolution Cu L_{23} XANES data of Sarma et al (48), as shown in Fig. 4. As expected this feature dominates for NaCuO$_2$ consistent with the Cu L_{23} XPS data. The separation of the d → p and pp* → cp features is found to be less than 1 eV in La and has relative intensities of around cp/c = 0.6 (48). This explains why it is not seen in the lower resolution EELS data in Fig. 4. For 123, the separation is 1.4 eV and cp/c is around 0.9 (48). The smaller energy separation in La compared with 123 is consistent with our theoretical model which predicts the separation to be $-\Delta + \delta_1 - \delta_1 + \beta$ = $-\Delta + 0.5$ eV. As Δ decreases from La to 123, the separation should get bigger. The pp* → cv contribution should increase at both core levels with doping level in La; however, it should increase much faster at the Cu L_{23} level since state 1) has more pp* character than dp. This is consistent with the EELS data, where the c and cp contributions are seen as one feature.

Temperature effects

Figure 2 summarizes the temperature effects which have been seen in the spectroscopic data for the high T_c materials (51-55). This data has been somewhat controversial, because it is not seen by all investigators. Nevertheless, it has been seen by several groups who have shown that it does not arise from increased impurities on the

surface at lower temperatures; e.g. these effects do not appear for the tetragonal 123 material, a non-HTSC, while they do appear for the orthorhombic 123 (54) which is a HTSC. Recent single crystal data (17,31) do not appear to exhibit similar effects, but they may yet be found since single crystals have not been thoroughly studied. If they indeed do not appear in the single crystal data, one might conclude that the grain boundaries in the sintered polycrystalline materials are somehow involved.

All of the temperature effects can be attributed to a single phenomenon, namely a decrease in c_p due to increased metallic screening (2) or long range polarization, which reduces U_{pe}. Thus the changes seen upon going from CuO to 123 simply continue upon lowering the temperature (2). This is consistent with the decrease in the main cp peak energy in the Cu 2p XPS, while the cd satellite remains unshifted (Figure 2a). The larger energy separation between the cd and cp states decreases the mixing which causes the satellite to decrease in intensity and the main peak to get narrower. Note that the primary cd peak does not shift in the O 1s XPS (Figure 2b), but a slight shift to lower energy is seen in the cp^p and cp^s contributions at lower temperature, as expected with a decrease in c_p. It is also consistent with the increase in the dp^2 satellite contribution in the Cu $L_{23}VV$ AES as shown in Figure 4c; since the dp^2 and d^2p states become closer in energy and hence mix more. However, no shift in the Auger kinetic energy of the principal peak is seen, this is because both the core hole cp and final d^2p states decrease together with c_p. Finally, the UPS spectra (not shown, see ref. 55) show a skewing toward the Fermi level at lower temperature, as expected with a decrease in c_p.

The intensity of the $pp^p \to cpp^p$ feature around 937 eV in the Cu XPS of Fig. 2b appears to decrease with temperature, although this is not clear. In other data (51,53,54), the breadth of the main peak clearly increases, and we attribute this to an increase in the $pp^p \to cpp^p$ contribution. Also note that the d $\to$ cp transition energy decreases with D, but the $pp^p \to cpp^p$ energy remains fixed, consistent with experiment. As the temperature is lowered, the charge carrier concentration or density of pp^p states apparently increases. This increase is consistent with the decrease in c_p due to increased metallic screening.

Finally, we should note that no temperature dependence has been seen in the EELS or XANES data (46-48). We note first that the energy of the primary d $\to$ c contribution does not involve Δ or c_p, so no shift is expected. We would expect an increase in the intensity of the $pp^p \to cp$ contribution as well as a small energy shift. Although this is has not been observed (48), it may be difficult to observe because this small contribution is barely resolved from the main feature. Furthermore, the electron excited in the absorption process can screen its own hole, since it generally remains on the same atom, so the long range polarization may be less important. Finally, the EELS and XANES data is more reflective of the bulk than the other spectroscopic data, and perhaps the surface alters the screening process.

The increased metallic like screening which appears to occur at lower temperature may indeed involve the grain boundaries, for it has been shown that the grain boundaries can strongly alter the conductivity and its dependence on temperature in these supercon-

ducting materials (56). Since this metallic screening occurs through electron-hole pair excitations at the Fermi level, the extent o* this screening is also expected to depend strongly on the DOS a* he Fermi level. It should also depend strongly on whether the sample is above or below the bulk T_c, however, insufficient data has been published to determine the exact nature of the temperature dependence around T_c. Evidence has been presented for granular superconductivity in 123 in the range 100 to 160 K, with the islands of coupled HTSC granules increasing in size as the temperature decreases (57). This could possibly contribute to the changes seen well above T_c.

Summary

We have reviewed the spectroscopic data for the high temperature superconductors, and compared them with that for CuO. We have summarized an interpretation of the data utilizing a highly correlated CuO_6 cluster model and show that a single set of Hubbard parameters predicts all of the state energies. Changes in the data between CuO and the HTSC's arises primarily from a reduction in ϵ_p; this reduction continues with decreasing temperature in the HTSC's due to increased metallic screening. Compared with CuO, the HTSC's show an increased covalent interaction between the Cu-O bonds. The large size of U_{pp}° and the temperature dependence reveal that metallic screening is incomplete, and hence that the DOS at the Fermi level in the HTSC's is relatively small.

Acknowledgments

Literature Cited

1.   Ramaker, D.E.; Turner, N.H.; and Hutson, F.L. submitted.
2.   Ramaker, D.E. submitted.
3.   Wendin, G. Proc. 14th Intl. Conf. on X-ray and Inner-Shell Processes, J. Physique (France)(In press).
4.   Anderson, P.W. Science 1987, 235, 1196.
5.   Varma, C.M.; Schmitt-Rink, S. E.; Abrahams, E. Sol.State. Commun. 1987, 62, 681.
6.   Doniach S. et al. In Novel Mechanisms of Superconductors, Wolf S.A. and Fresin V.Z. Ed.; Plenum: NY, 1987, p 395.
7.   Hirsch, J.E. et al. Phys. Rev. Letters 1988, 60, 1168.
8.   vanderLaan G. et al. Phys. Rev. 1981, 24, 4369.
9.   Fuggle J.C. et al. Phys. Rev. 1988, B37, 1123.
10. Greedan J.E. et al. Phys. Rev. 1987, B35, 8770.
11. de Groot, R.A.; Gutfreund, H.; Weger, M. Sol. State Commun. 1987, 63, 451.
12. Folkerts, W. et al. J. Phys. C: Solid State Phys. 1987, 20, 4135.
13. Manthiram, A.; Tang, X.X.; Goodenough, J.B. Phys. Rev. 1988, B37, 3734.
14. Redinger, J. et al. Phys. Lett. 1987, 124, 463 and 469.
15. Thuler, M.R.; Benbow, R.L.; Hurych, Z. Phys. Rev. 1982, B26, 669.

16. Benndorf, C. et al. J. Electron. Spectrosc. Related Phenom. 1980, 19, 77 .
17. Stoffel, N.G. et al. Phys. Rev. 1988, B37, 7952; also preprint.
18. Kurtz, R. et al. Phys. Rev. 1987, B35, 8818.
19. Mueller, D. et al. In ref. 6, p 829.
20. Onellion, M. et al. Phys. Rev. 1987, B36, 819.
21. Tang, M. et al. Phys. Rev. 1988, B37, 1611; also preprint.
22. Samsavar, A. et al. Phys. Rev. 1988, B37, 5164.
23. Rosencwaig, A.; Wertheim, G.K. J. Elect. Spectrosc. Related Phenom. 1972/73, 1, 493.
24. Miller, D.C. et al. In Thin Film Processing and Characterization of High Temperature Superconductors, Harper, J.M.; Colton, J.H.; and Feldman, L.C. Eds., AVS Series No. 3, American Institute of Physics: New York, NY, 1988; p 336.
25. Steiner, P. et al. Appl. Phys. 1987, A44, 75.
26. Weaver, J. et al. preprint.
27. Reihl, B. et al. Phys. Rev. 1987, B35, 8804.
28. Klopman, G. J. Am. Chem. Soc. 1964, 86, 4550.
29. Brewer J.H. et al. Phys. Rev. Lett. 1988, 60, 1073.
30. Chang, Y. et al. preprint; Onellion, M. et al. preprint.
31. Takahashi T. et al. Phys. Rev. 1988, B37, 9788.
32. Kohiki, S.; Hamada, T. Phys. Rev. 1987, B36, 2290.
33. Ramaker, D.E. et al. Phys. Rev. 1987, 36, 5672.
34. Sarma, D.D. Phys. Rev. 1988, B37, 7948.
35. Steiner, P. et al. Z. Phys. B- Condensed Matter 1987, 67, 497.
36. Steiner, P. et al. Z. Phys. B- Condensed Matter 1988, 69, 449.
37. Gourieux, T. et al Phys. Rev. 1988, B37, 7516.
38. Qiu, S.L. et al. Phys. Rev. 1988, B37, 3747.
39. Ford, W.K. et al. Phys. Rev. 1988, B37, 7924.
40. Ramaker, D.E.; Turner, N.H.; Hutson, F.L. In Ref. 24, p 284.
41. van der Marel, D. et al. Phys. Rev. 1988, B37, 5136.
42. Fiermans, L.; Hoogewijs, R.; Vennik, J. Surf. Sci. 1975, 47, 1.
43. Chang, Y. et al. Phys. Rev. B (In press).
44. Tsang, K.L. et al. Phys. Rev. 1988, B37, 2293.
45. Koster, A.S. Mole. Phys. 1973, 26, 625.
46. Nucker, N. et al. Z. Phys. B: Cond. Matter 1987, 67, 9; Phys. Rev. 1988, 37, 5158.
47. Bianconi, A. et al. Solid State Commun. 1987, 63, 1009; Intn. J. Modern Phys. 1987, 131, 853.
48. Sarma, D.D. et al. Phys. Rev. 1988, B37, 9784.
49. Ramaker, D.E. Phys. Rev. 1982, B25, 7341.
50. Erickson, N.E.; Powell, C.J.; Ramaker, D.E. Phys. Rev. Letters 1987, 58, 507.
51. Dauth, B. et al. Z. Phys. B- Condensed Matter 1987, 68, 407.
52. Balzarotti, A. et al. Phys. Rev. 1987, B36, 8285.
53. Sarma, D.D. et al. Phys. Rev. 1987, B36, 2371.
54. Kim, D.H. et al. Phys. Rev. 1988, B37, 9745.
55. Iqbal, Z. et al. J. Materials. Res. 1987, 2, 768.
56. Renker, B. et al. Z. Phys. B- Cond. Matter 1987, 67, 1.
57. Cai, X.; Joynt, R.; Larbalestier, D.C. Phys. Rev. Letters 1987, 58, 2798.

TECHNICAL REPORT DISTRIBUTION LIST, GEN

	No. Copies		No. Copies
Office of Naval Research Attn: Code 1113 800 N. Quincy Street Arlington, Virginia 22217-5000	2	Dr. David Young Code 334 NORDA NSTL, Mississippi 39529	1
Dr. Bernard Douda Naval Weapons Support Center Code 50C Crane, Indiana 47522-5050	1	Naval Weapons Center Attn: Dr. Ron Atkins Chemistry Division China Lake, California 93555	1
Naval Civil Engineering Laboratory Attn: Dr. R. W. Drisko, Code L52 Port Hueneme, California 93401	1	Scientific Advisor Commandant of the Marine Corps Code RD-1 Washington, D.C. 20380	1
Defense Technical Information Center Building 5, Cameron Station Alexandria, Virginia 22314	12 high quality	U.S. Army Research Office Attn: CRD-AA-IP P.O. Box 12211 Research Triangle Park, NC 27709	1
DTNSRDC Attn: Dr. H. Singerman Applied Chemistry Division Annapolis, Maryland 21401	1	Mr. John Boyle Materials Branch Naval Ship Engineering Center Philadelphia, Pennsylvania 19112	1
Dr. William Tolles Superintendent Chemistry Division, Code 6100 Naval Research Laboratory Washington, D.C. 20375-5000	1	Naval Ocean Systems Center Attn: Dr. S. Yamamoto Marine Sciences Division San Diego, California 91232	1

ABSTRACTS DISTRIBUTION LIST, 056/625/629

ABSTRACTS DISTRIBUTION LIST, 056/625/629

Dr. J. E. Jensen
Hughes Research Laboratory
3011 Malibu Canyon Road   -
Malibu, California 90265

Dr. J. H. Weaver
Department of Chemical Engineering
  and Materials Science
University of Minnesota
Minneapolis, Minnesota 55455

Dr.-A. Reisman
Microelectronics Center of North Carolina
Research Triangle Park, North Carolina
  27709

Dr. M. Grunze
Laboratory for Surface Science
and Technology
University of Maine
Orono, Maine 04469

Dr. J. Butler
Naval Research Laboratory
Code 6115
Washington D.C. 20375-5000

Dr. L. Interante
Chemistry Department
Rensselaer Polytechnic Institute
Troy, New York 12181

Dr. Irvin Heard
Chemistry and Physics Department
Lincoln University
Lincoln University, Pennsylvania 19352

Dr. K. J. Klaubunde
Department of Chemistry
Kansas State University
Manhattan, Kansas 66506

Dr. C. B. Harris
Department of Chemistry
University of California
Berkeley, California 94720

Dr. R. Bruce King
Department of Chemistry
University of Georgia
Athens, Georgia 30602

Dr. R. Reeves
Chemistry Department
Renssaeler Polytechnic Institute
Troy, New York 12181

Dr. Steven M. George
Stanford University
Department of Chemistry
Stanford, CA 94305

Dr. Mark Johnson
Yale University
Department of Chemistry
New Haven, CT 06511-8118

Dr. W. Knauer
Hughes Research Laboratory
3011 Malibu Canyon Road
Malibu, California 90265

Dr. Theodore E. Madey
Surface Chemistry Section
Department of Commerce
National Bureau of Standards
Washington, D.C. 20234

Dr. J. E. Demuth
IBM Corporation
Thomas J. Watson Research Center
P.O. Box 218
Yorktown Heights, New York 10598

Dr. M. G. Lagally
Department of Metallurgical
  and Mining Engineering
University of Wisconsin
Madison, Wisconsin 53706

Dr. R. P. Van Duyne
Chemistry Department
Northwestern University
Evanston, Illinois 60637

Dr. J. M. White
Department of Chemistry
University of Texas
Austin, Texas 78712

Dr. Richard J. Saykally
Department of Chemistry
University of California
Berkeley, California 94720

ABSTRACTS DISTRIBUTION LIST, 056/625/629